



Dynamic Shear Fracture Behaviour of Granite Under Axial Static Pre-force by 3D High-Speed Digital Image Correlation

Chenxi Zhang¹ · Diyuan Li¹ · Jinyin Ma¹ · Quanqi Zhu¹ · Pingkuang Luo¹ · Yuda Chen¹ · Minggang Han¹

Received: 28 July 2022 / Accepted: 19 July 2023 / Published online: 31 July 2023
© The Author(s), under exclusive licence to Springer-Verlag GmbH Austria, part of Springer Nature 2023

Abstract

The investigation on dynamic shear fracture behaviour of rocks subjected to the simulated geo-stress is of great importance for deep rock engineering. Four groups of dynamic mode II fracture tests with different axial pre-forces were conducted on the granite short core in compression (SCC) specimens using a coupled static–dynamic loading system. It can be found that dynamic mode II fracture toughness rises with increasing loading rate at a given pre-force ratio and decreases with increasing pre-force ratio at a given loading rate. Total fracture toughness exhibits evident rate dependence and it is almost independent of the pre-forces. An empirical model was established to describe the influence of the pre-force and loading rate on the Mode II fracture toughness. Deformation, damage and fracture characteristics of rock were elaborated based on surface deformation field. The results indicate that (1) The original damage caused by pre-force increases with the pre-force ratio; (2) The fracture path is independent of pre-force ratio and the loading rate in the studied range; (3) At a given pre-force ratio, the loading rate has a significant effect on the final failure pattern of the SCC specimen. In addition, a novel relative shear velocity (RSV), defined as the ratio of relative shear displacement and time spent from deformation onset to the generation of complete shear fracture, is proposed to depict the dynamic shear crack propagation. The results indicate that the RSV increases with loading rate irrespective of the pre-force, showing a power function relationship with loading rate.

Highlights

- Dynamic mode II fracture tests were conducted on the granite short core in compression specimens using a coupled static–dynamic loading system.
- The relationship between dynamic mode II fracture toughness with axial pre-force and loading rate is analysed qualitatively and quantitatively.
- Deformation, damage and fracture features of granite were elaborated using three-dimensional high-speed digital image correlation technique.
- A novel index, relative shear velocity, based on surface displacement field, is proposed to depict the dynamic shear crack propagation.

Keywords Dynamic mode II fracture toughness · Pre-force · Short core in compression · 3D digital image correlation · Relative shear velocity

1 Introduction

Fracture mechanics is the scientific principle and method to study the ability of solid material to resist initiation and propagation of internal crack under external force (Ayatollahi and Aliha 2011; Li et al. 2022). This ability is described as critical stress intensity factor (SIF) or fracture toughness in linear elastic fracture mechanics, which is often

✉ Diyuan Li
diyuan.li@csu.edu.cn

¹ School of Resources and Safety Engineering, Central South University, Changsha, China

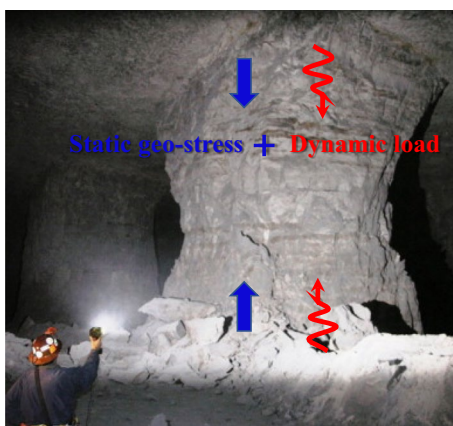


Fig. 1 The representative stress state of pillars in subsurface mine (Esterhuizen et al. 2011)

subdivided into mode I, mode II and mode III on the basis of the different fracture mode (Erdogan and Sih 1963; Pook 1971; Awaji and Sato 1978; Li et al. 2022; Wu et al. 2021). Recently, fracture mechanics theory has been widely applied to many engineering scenarios for the prevention of fracture growth to improve structural stability, e.g. rock slopes and underground cavities (Backers and Stephansson 2012), and the employment of fracture to enhance rock-breaking efficiency, e.g. hydraulic fracturing and tunnel boring (Du et al. 2020, 2021; Wei et al. 2016).

It is recognised that opening fractures are commonly dominant fracture mode in brittle or quasi-brittle rock materials because of the fact that tensile strength of rocks is usually less than their shear strength (Yin et al. 2021). Therefore, the dynamic mode I fracture properties of rock materials are extensively studied. Despite different methods to obtain dynamic mode I fracture toughness were used, the effects of dry–wet cycles (Cai et al. 2020), freeze–thaw cycles (Niu et al. 2021), high temperature (Yin et al. 2012, 2022), moisture content (Zhou et al. 2019b) and loading rate (Zhang et al. 1999, 2000) on dynamic mode I fracture parameters under dynamic loading all show similar laws, such as the rate effect of dynamic fracture toughness, the weakening effect of these external factors on the crack initiation resistance of rock.

The above studies reveal the dynamic opening fracture properties of rocks subjected to only single impact, which are actually fundamental research work. Whereas, it is well known that structure stability of rock engineering, e.g. pillars in underground mine (Esterhuizen et al. 2011) as shown in Fig. 1, is affected jointly by static high geo-stress and dynamic loads caused by blasting operations, drilling or sudden earthquakes (Yin et al. 2022; Zhou et al. 2014, 2020; Zhu et al. 2022b). Moreover, natural rocks often contain numerous defects, such as joints and fissures, which are also

important factors affecting the stability of underground engineering structures (Wei et al. 2017). Hence, it is important to conduct related researches on dynamic fracture behaviour of cracked rocks under joint actions of pre-existing static stress and impact loading for the safety and stability analysis of structures in rock engineering (Li et al. 2008; Yin et al. 2022). It should be noted that engineered rock masses, due to the influence of structural surfaces, often exhibit many differences in mechanical properties and behaviour from rock materials used in the laboratory. This involves a scaling problem that remains to be further studied, which is beyond the scope of this study.

Some works have been carried out to investigate dynamic tensile fracture behaviour of rocks and rock-like materials under coupled dynamic–static loads. Chen et al. (2016), Shi and Chen (2018) and Han et al. (2022b) conducted the dynamic opening fracture tests on different solid materials under coupled dynamic and static loading using semi-circular bending (SCB) specimens. The results showed that the dynamic and total fracture toughness of two materials reveal obvious rate effect. However, the variation in fracture toughness induced by the increasing pre-stress exhibits a contradictory trend. This may be related to the differences in the solid materials used in their experiments and the methods to process experimental data. Yao et al. (2019), Zhou et al. (2014) and Wu et al. (2015) investigated the effect of pre-tension stress and loading rate on dynamic tensile strength of rock using the SCB and Brazilian disc (BD) methods. The results suggested that the dynamic tensile strength of rock increased with the growth in loading rate at the same pre-stress and went down with the augmenting pre-stress under a similar loading rate, whereas the total tensile strength seemed to have no connexion with the pre-stress. The above studies mainly focus on the effects of pre-existing static loads and loading rate on fracture toughness and strength values and final failure patterns, whereas little attention is paid to the fracture process and the surface deformation field as well as the damage process under coupled dynamic and static loads, which is indispensable to reveal further fracture characteristics under combined dynamic and static load.

Studies on dynamic mode II fracture are rarely conducted under the joint action of dynamic and pre-applied static stress because of the complexity of shear fracture itself. Nevertheless, there is no doubt that mode II fracture still occurs frequently under high confining pressure (Bahrami et al. 2022), which is strongly related to the stability of jointed rock masses (Yin et al. 2021). A punch-shear method for measure of the static shear fracture toughness of rocks was proposed by Backers et al. (2002), which became the suggested method by the International Society for Rock Mechanics (ISRM) due to its effectiveness (Backers and Stephansson 2012). To further extend this method to the

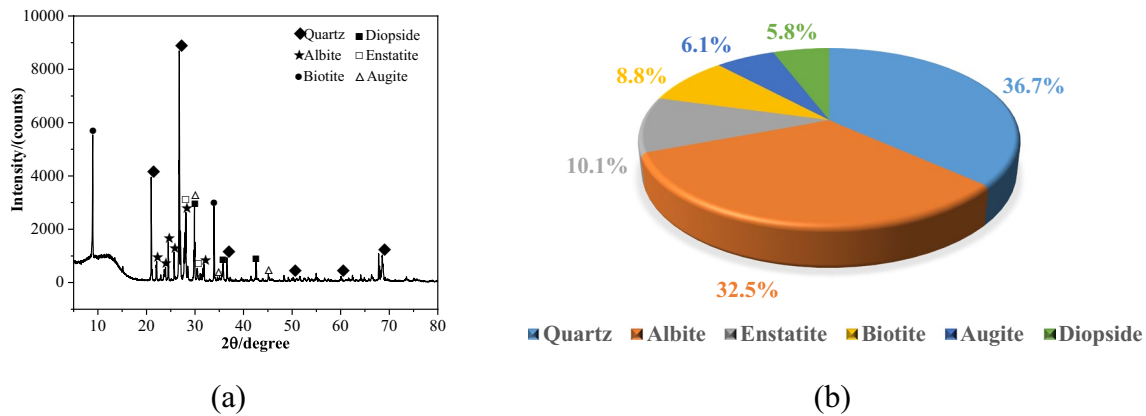


Fig. 2 The outcomes from the XRD analysis. **a** Spectrum; **b** content of components

dynamic field, Yao et al. (2017) modified the geometry of PTS (punch-through shear) specimens to fulfil the dynamic stress equilibrium and then the rate effect and confining pressure effect of dynamic shear fracture toughness was studied (Yao et al. 2020). The results showed that the dynamic shear fracture toughness increased with raising loading rate and confining pressure. Yin et al. (2021) examined the temperature effect of dynamic shear fracture toughness for rock using this method. Yao et al. (2021b) investigated the effect of hydrostatic pressure on dynamic mode II fracture behaviour using SCC method. The results indicated the dynamic mode II fracture toughness positively correlated with the rising loading rate and was almost unaffected by hydrostatic pressure at a similar loading rate. Zhang et al. (2023) have carried out a series of dynamic SCC tests recently. The crack extension path, the displacement field evolution and the morphological features of dynamic mode II fracture under single impact were investigated and analysed.

The above researches have laid the foundation for understanding the dynamic shear fracture characteristics of rocks. However, there are few studies on dynamic mode II fracture properties of rocks subjected to coupled dynamic–static loads. Considering the importance of dynamic shear fracture behaviour in deep rock engineering, it is quite necessary to conduct an in-depth study on this fracture mode of rock materials subjected to combined dynamic–static loads. To prepare specimens expediently and observe the shear fracture band on the specimen surfaces, the SCC approach is used to determine dynamic shear fracture toughness under varying loading rates and static pre-force in the present study. In addition, the 3D-DIC (three-dimensional digital image correlation) technique was adopted to record the apparent deformation field and the dynamic fracture process of the SCC specimens during entire loading.

2 Experimental Methodology

2.1 Material Description and Preparation

In the present tests, granites taken from a stone quarry in Zhangzhou city, China, were selected as the tested materials. The rock petrographic analysis showed the grain size of Zhangzhou granite used in this work is in the range of 0.01–1.2 mm and thus the rock was classified as a fine-grained granite. As shown in Fig. 2, the outcomes of X-ray diffraction (XRD) analysis display the granite is mainly composed of 32.5% albite, 36.7% quartz, 10.1% enstatite, 8.8% biotite, 6.1% augite and 5.8% diopside by weight. The wave velocity c , density ρ , Young's modulus E , Poisson's ratio λ and Brazilian tensile strength σ_t of granite are measured as 5131.56 m/s, 2784.16 kg/m³, 40.16 GPa, 0.31 and 11.3 MPa respectively.

Figure 3 shows the geometric configuration and the photographic image of SCC specimen captured from high-speed camera. This specimen is a cylindrical piece with 50 mm in diameter D and 50 mm in height H , and has two notches with a depth a of 25 mm and a thickness t of 1 mm as well as a vertical distance C of 10 mm. Figure 3c illustrates stress condition of specimen in tests, which is in coordination with that in Fig. 1.

2.2 Experimental Setup

Figure 4 shows the overview of the testing system used in this work. The dynamic tests, both without and with pre-stress, were performed on the modified split Hopkinson pressure bar (SHPB) system that allows axial static and dynamic loads to be applied sequentially to the same specimen in a single test. Obviously, the experimental compositions mainly consist of a combined dynamic–static loading system and a high-speed 3D-DIC system.

Fig. 3 The SCC specimen: **a** Geometry; **b** digital image; **c** stress state

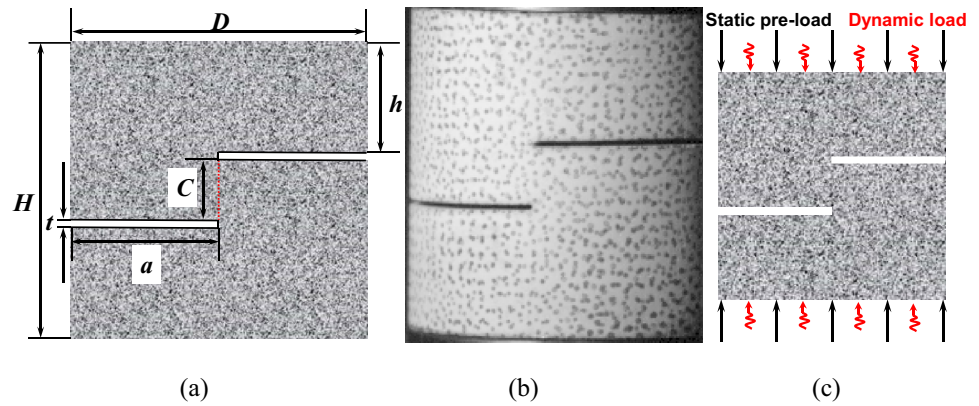
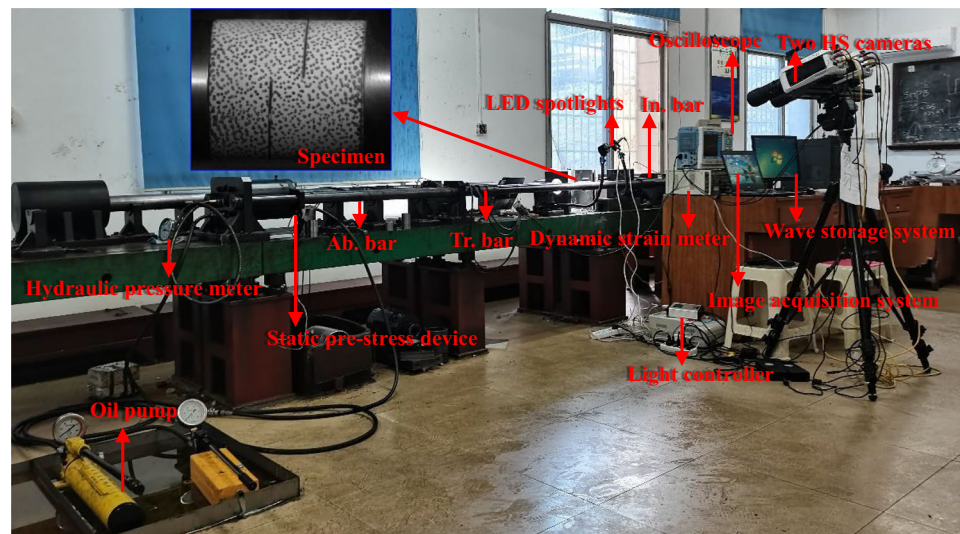


Fig. 4 The complete testing system



2.2.1 Coupled Dynamic–Static Loading System

The loading system incorporates a striker launcher and three aligned bars, namely an incident, a transmitted and an absorption bars, some apparatus for applying axial prestress and a waveform collection system (a SDY2107A ultradynamic strain metre linked to a DL850E digital oscilloscope). For more detailed knowledge of this device, please refer to (Li et al. 2008) and (Han et al. 2022a).

In coupled static–dynamic tests, some Vaseline was smeared evenly on the end faces of the specimen to reduce the friction effect before SCC specimens were clamped between the incident bar (In.bar) and transmitted bar (Tr. bar). The axial static pre-force was then applied slowly by the static pre-stress loading device with a manual oil pump until a predetermined value was reached. Next, the cone-shaped striker subjected to pre-pressurised nitrogen gas was launched from the pressure container after unscrewing the gas valve and impacted on the incidence bar to engender a half-sine wave. Once the pulse signal produced by

the stress waves reaches the trigger threshold of -20 mv, it will be collected by two strain gauges conglutinated on the incident and transmitted bars then recorded by the oscilloscope. Applicability and validity of the one-dimensional wave theory in combined dynamic–static loading tests had been proved theoretically by Li et al. (2008). Hence, the axial dynamic stress $\sigma(t)$, strain $\varepsilon(t)$ and strain rate $\dot{\varepsilon}(t)$ are derived as (Han et al. 2022c):

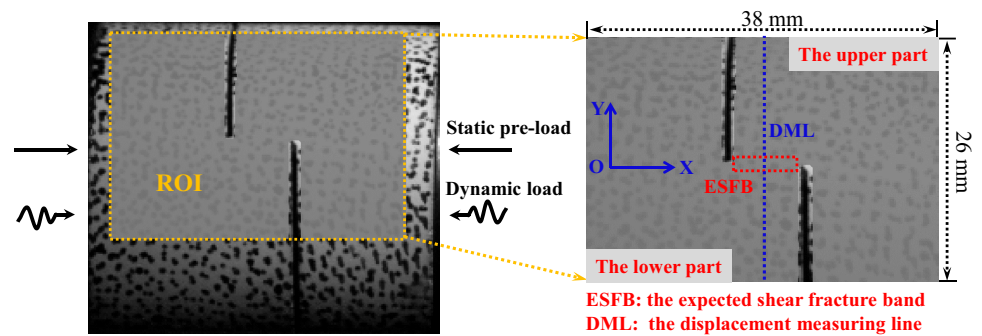
$$\sigma(t) = \frac{A_e E_e}{2A_s} [\varepsilon_I(t) + \varepsilon_R(t) + \varepsilon_T(t)] \quad (1)$$

$$\varepsilon(t) = \frac{C_e}{L_s} \int_0^t [\varepsilon_I(t) - \varepsilon_R(t) - \varepsilon_T(t)] dt \quad (2)$$

$$\dot{\varepsilon}(t) = \frac{C_e}{L_s} [\dot{\varepsilon}_I(t) - \dot{\varepsilon}_R(t) - \dot{\varepsilon}_T(t)] \quad (3)$$

where A_e , E_e and C_e represent the end area, elastic modulus and P-wave velocity of cylindrical bars; A_s and L_s denote the

Fig. 5 The ROI and the expected shear fracture band (ESFB) in specimen



contact area between specimen and bars, and length of the specimen; $\varepsilon_I(t)$, $\varepsilon_R(t)$ and $\varepsilon_T(t)$ express the incident, reflected and transmitted strain pulses respectively.

2.2.2 3D Digital Image Correlation (DIC) System

The DIC technique is a non-contact method for measuring the deformation field on the surface of solid materials and has been often employed to depict the crack extension and fracture process in flawed rock (Li et al. 2022; Ma et al. 2022; Zhou et al. 2019a; Zhu et al. 2022a). The 2D DIC method is usually used to monitor in-plane deformation fields of materials and it is required that the camera lens is perpendicular to the observation surface of the specimens (Munoz et al. 2016; Zhu et al. 2022b). Two prominent advantages of 3D method compared to the 2D method are that it has the capable of observing out-of-plane deformation and surface deformation of curved specimens (Munoz and Taheri 2017; Munoz et al. 2016; Tang et al. 2012). Hence, 3D DIC method was selected in the study considering that the observed surface for the SCC specimen was cylindrical. The 3D-DIC system contains two LED spotlights, two high-speed (HS) cameras and image acquisition system, as shown in Fig. 4. Two HS cameras with a resolution of 256×256 pixels and a frequency of 74,544 fps (frames per second) were applied to record the speckle patterns on the specimen surface under original and loaded states. Two LED spotlights were employed for exposure compensation and light brightness can be adjusted by a light controller. Stereo camera calibration is crucial work for 3D DIC method, which is directly related to the 3D reconstruction accuracy (Tang et al. 2012). The calibration was conducted to acquire some intrinsic parameters, e.g. lens distortion factor and extrinsic spatial position of the two HS cameras. In order to calibrate these parameters, a series of calibration images were obtained by moving, rotating, and tilting a calibration board in front of the specimen (Xing et al. 2018) and an acceptable calibration precision was achieved eventually in the three-dimensional visual image correlation (VIC-3D) software. The digital images captured during experiments were then analysed via VIC-3D software. The deformation information

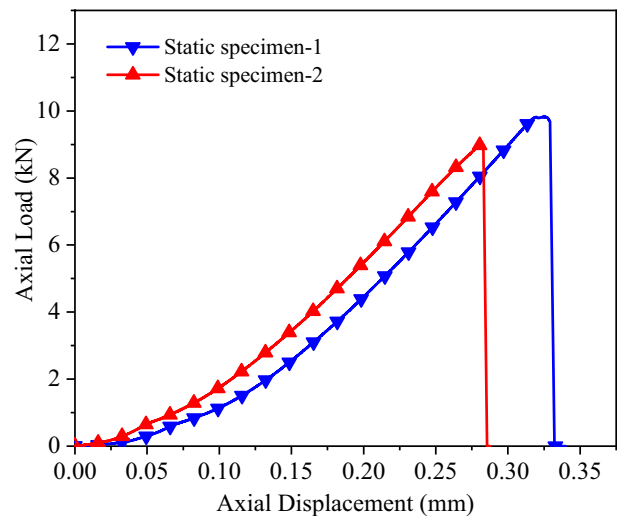


Fig. 6 Recordings of axial load–displacement for SCC specimens in static uniaxial compression tests

recorded in the digital images is then analysed and obtained by the VIC-3D software. As shown in Fig. 5, the region of interest (ROI) delineated on the observation surface is rectangle with 38 mm in length and 26 mm in width.

2.2.3 Determination of Static Pre-force

Before conducting the combined dynamic–static impact tests, two static SCC tests were conducted to obtain the static peak load of the SCC specimens as the basis for the subsequent setting of the pre-shear force. As shown in Fig. 6, the static peak load for two SCC specimens is measured as 5.004 MPa and 4.594 MPa respectively and its average value is 4.8 MPa. In this study, we plan to perform four sets of coupled dynamic and static fracture tests with different pre-force and thus value of four pre-force can further be determined as 0 MPa, 1.2 MPa, 2.4 MPa and 3.6 MPa. These pre-force values account for 0, 0.25, 0.5 and 0.75 of the static peak force respectively, which is defined as the axial pre-force ratio (APFR) in the study.

Table 1 The relation between the oil pressure and the static load in the bar

Static pre-force (kN)	Axial pre-force ratio	Oil pressure (MPa)			
		Group-1	Group-2	Group-3	Ave
0	0	0	0	0	0
2.356	25%	0.25	0.21	0.20	0.22
4.712	50%	0.44	0.42	0.42	0.43
7.068	75%	0.65	0.64	0.66	0.65

To ensure the consistency of the load in the bar with the preset load in subsequent tests, the former is calibrated with the oil pressure in the device for applying axial pressure. The specific operation steps are as follows: (1) the pressure sensor was first sandwiched between the incident and the transmitted bars, through which the load in the bars in real time could be known; (2) axial pressure was slowly applied by the manual oil pump and its magnitude could be read out from the oil pressure metre; (3) in this way, once the load in the bar reaches the preset pre-force, the value of oil pressure would be recorded. The results after three calibrations are listed in Table 1. The average of oil pressure, e.g. 0 MPa, 0.22 MPa, 0.43 MPa and 0.65 MPa, corresponding to different pre-force values in calibration results, was used in experiments.

3 Results

3.1 DIC Calibration

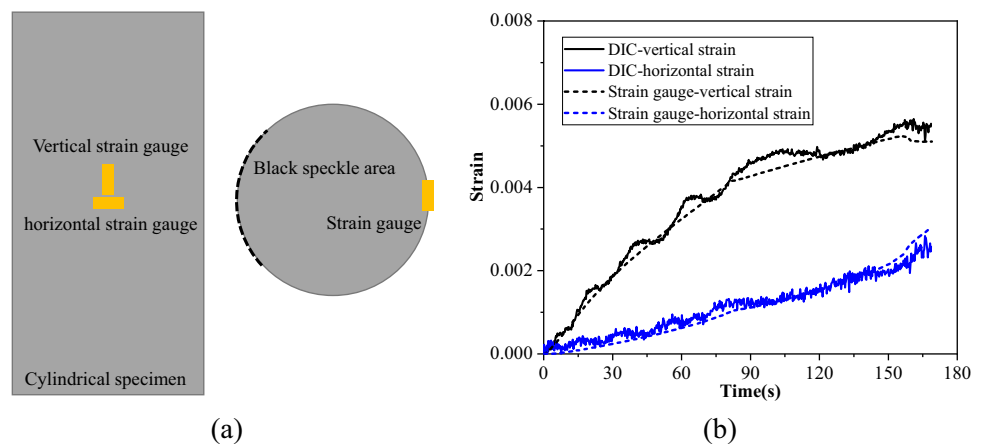
When the VIC-3D software was used for surface deformation analysis of solid materials, some parameters, such as subset, step, filter size, etc., are very important for the accuracy of DIC results (Aliabadian et al. 2019; Li et al. 2021a, b). To obtain the optimal combination of parameters, different DIC parameters were set for the

deformation analysis of cylindrical specimens under uniaxial compression loading. Figure 7a shows the location of two strain gauges and black speckle area or observation area of DIC. Two inspect rectangles with similar dimensions to the strain gauges in the backside of the specimen were laid and then vertical strain as well as horizontal strain in the rectangle centre were extracted. The results are shown in Fig. 7b. It can be seen that the DIC results, obtained using this combination of parameters for strain analysis (subset = 23 step = 1, filter size = 9), are in good agreement with the strain gauge data. Note that the results of deformation analysis of other specimens are all obtained using this parameter combination.

3.2 Detection for Dynamic Stress Balance

As stated in the method recommended by the ISRM, achieving dynamic stress equilibrium at both ends of the specimen prior to failure is the required precondition for an effective dynamic test (Zhou et al. 2012), which can be examined through matching the dynamic stress histories during loading process. Once dynamic stress equilibrium was accomplished in tests, dynamic fracture toughness can be computed by substituting the dynamic peak loads obtained from the impact tests into the quasi-static equation (Dai et al. 2010; Yao et al. 2017, 2021b). Recently, the problem of dynamic force balance was well addressed in dynamic shear fracture tests based on the modified PTS method and SCC method (Yao et al. 2017, 2021b), which contributed to the understanding of mode II fracture behaviour of rock under impact load. Figure 8 illustrates the stress–time curves in a representative impact test. Clearly, the sum of incident and reflected stresses is roughly equivalent to the transmitted stress, indicating an axial dynamic stress balance is well realised and the dynamic stress across the specimen is almost uniform.

Fig. 7 **a** Location of strain gauges; **b** comparison of DIC results and strain gauge results



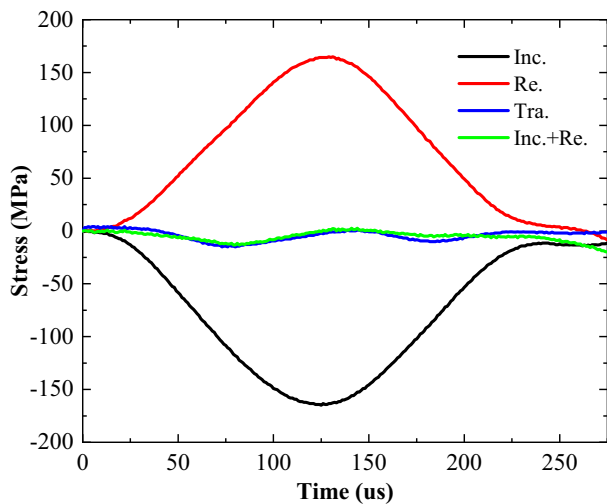


Fig. 8 A typical dynamic stress balance in SCC-SHPB tests. *Inc* incident wave, *Re* reflected wave, *Tra* transmitted wave

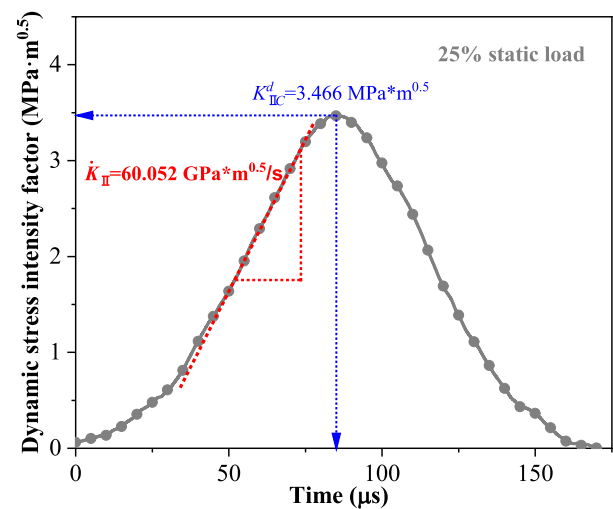


Fig. 9 the DSIF–time curve for a representative SCC specimen with the 0.25 of pre-force ratio

3.3 Dynamic Fracture Toughness

In SHPB-SCC tests, after dynamic stress balance is attained, the dynamic stress intensity factor (DSIF) history in the SCC specimen can be computed by (Zhang 2019):

$$K_{II}(t) = \left(0.7626 \frac{C}{H} + 0.0893 \right) \frac{P(t)}{DC} \sqrt{\pi a} \quad (4)$$

where $P(t)$ denotes the changing dynamic force in specimen with time.

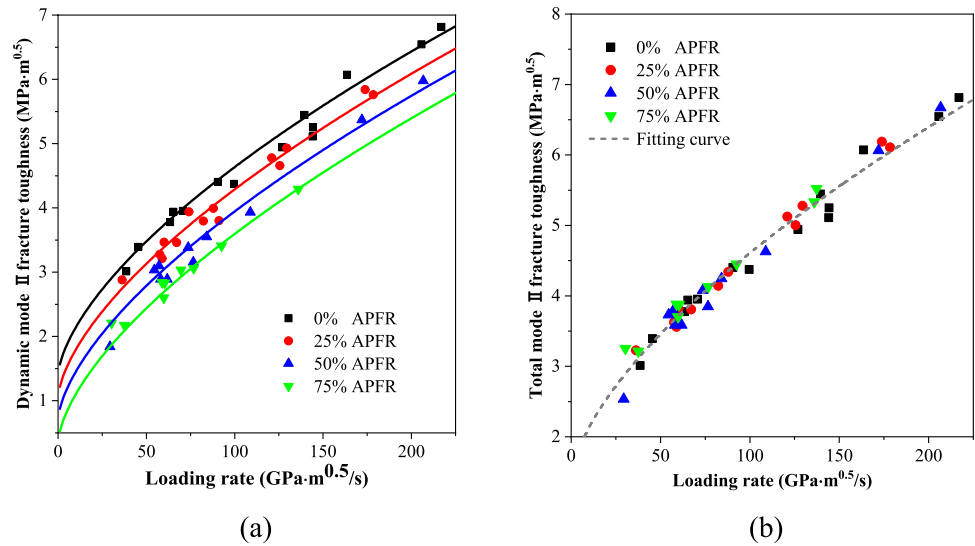
Conforming to the illustration for loading rate in the method suggested by ISRM (Zhou et al. 2012), the slope of linearly increasing segment before the failure point in the DSIF–time curve denotes the loading rate in a SHPB-SCC test. The determination of the loading rate for a typical SCC specimen is displayed in Fig. 9.

In this study, two types of mode II fracture toughness, namely dynamic mode II fracture toughness K_{II}^d and total mode II fracture toughness K_{II}^{tot} of rock, are considered. The former directly originates from dynamic peak force and the latter is the sum of the static SIF K_{II}^s produced by the axial pre-force and the dynamic mode II fracture toughness K_{II}^d . The force substituted into the Eq. (4) for determining K_{II}^d and K_{II}^{tot} is the peak dynamic force P_d and the total force P_{tot} on SCC specimens, namely the sum of P_d and the axial static pre-force P_s . Hence, it can be seen clearly that K_{II}^d describes the capacity to resist the shear crack propagation for rock already subjected to a certain static pre-load under dynamic impact, whereas K_{II}^{tot} represents the total resistance of rock to shear crack expansion under coupled static–dynamic loads.

Figure 10 demonstrates the relations between K_{II}^d and K_{II}^{tot} , and the loading rate for varying pre-forces. It is clear

that both K_{II}^d and K_{II}^{tot} all increase with the increasing loading rate, implying that the rate-dependency of rock shear fracture toughness like the other properties of rock or rock-like materials, e.g. dynamic mode I fracture toughness (Zhang et al. 1999), compression strength (Zhou et al. 2020) and indirect tensile strength (Cho et al. 2003). In addition, it is observed from Fig. 9a that the K_{II}^d of granite decreases with the growth in static pre-force at given the loading rate. For instance, as the loading rate reaches about 60 GPa·m^{0.5}/s, the K_{II}^d of SCC granite specimen is calculated as 3.777 MPa·m^{0.5} under circumstance of no pre-force. Nevertheless, the K_{II}^d of the tested rock at similar loading rate are measured as 3.466 MPa·m^{0.5} in case of 25% APFR, 3.1 MPa·m^{0.5} with 50% APFR and 2.832 MPa·m^{0.5} with 75% APFR respectively. It can be seen in Fig. 6 that a significant nonlinearity is observed in the initial stage for static load–displacement curve owing to the heterogeneity of the microstructures in rocks (Peng et al. 2020). The previous interpretation regarding the concave period in the uniaxial stress–strain curves of intact rocks, e.g. micro-cracks closure, is no more available since rock at the notch tips is subjected to shear stress (Zhang et al. 2022). It can be interpreted as the fact that some micro-cracks commences in the micro-scale weak interfaces that are distributed randomly at the ESFB and then lentamente develop, but the energy stored in rock is not adequate to create an overall fracture surface (Zuo et al. 2013). With the increase of APFR, more micro-cracks generate and gather in the ESFB and the damage level in rock micro-structure raises, which weakens the resistance of SCC specimen to shear crack expansion under dynamic impact load. Hence, crack propagation in the SCC specimen can

Fig. 10 The influence of loading rate on **a** the dynamic mode II fracture toughness and **b** the total mode II fracture toughness with different APFRs



be triggered by a diminished dynamic force. Some scholars also have observed similar trend for dynamic toughness and strength in tensile mode for rock and concrete under pre-tension (Chen et al. 2016; Wu et al. 2015; Yao et al. 2019).

Figure 10b shows that the K_{IIC}^{tot} of SCC specimen almost keep constant at the similar loading rate irrespective of the applied axial static pre-force to SCC specimen, which implies that K_{IIC}^{tot} determined by SCC method is insensitive to the changes in the axial pre-force. It can be interpreted that a higher pre-force produced more activated microcracks in specimen, which enhance the viscosity of the rock and make it more sensitive to the loading rate. The weakening influence of pre-force on the dynamic fracture properties of the rock is counteracted by this increased sensitivity to the loading rate. Therefore, total mode II fracture toughness features approximately the independence of pre-shear force. In addition, this may indicate that the total resistance of the rock to shear fracture is approximately fixed and will be greatly deteriorated under the action of larger pre-load. Accordingly, the ultimate shear fracture can be incurred by a puny dynamic load in this case.

3.4 Empirical Relationship for Fracture Toughness

It can be found that both the loading rate and the axial pre-force have a substantial effect on the shear fracture toughness of rock. In this part, we attempt to establish an empirical model to describe the complicated relationship amongst them. Based on the results of the dynamic SCB method

(Chen et al. 2016; Yao et al. 2019) and general trend of fracture toughness in the study as affected by loading rate and axial pre-force, the empirical formulas are put forward:

$$\frac{K_{IIC}^d}{K_{IIC}^s} = f_d \left(\frac{K_{II}^s}{K_{IIC}^s}, \frac{\dot{K}_{II}}{\dot{K}_{II}^s} \right) = 1 - \left(\frac{K_{II}^s}{K_{IIC}^s} \right) + \alpha \left(\frac{\dot{K}_{II}}{\dot{K}_{II}^s} \right)^\beta \quad (5)$$

where K_{II}^s represents the stress intensity factor induced by the axial pre-force, K_{IIC}^s is the static mode II fracture toughness (here $K_{IIC}^s = 1.39 \text{ MPa}\cdot\text{m}^{0.5}$), \dot{K}_{II} denotes the loading rate in tests, $\dot{K}_{II}^s (= K_{IIC}^s/1s)$ denotes the static or reference loading rate, α and β are two fitting parameters. The pre-force effect is reflected by the second term (K_{II}^s/K_{IIC}^s) in Eq. (5) and the third term $\alpha(\dot{K}_{II}/\dot{K}_{II}^s)^\beta$ expressed the rate-dependency of dynamic shear fracture toughness. On the one hand, when no pre-force is applied to the specimen, the value of K_{II}^s is zero and thus Eq. (5) can be simplified further to $K_{IIC}^d/K_{IIC}^s = 1 + \alpha(\dot{K}_{II}/\dot{K}_{II}^s)^\beta$. On the other hand, at a loading rate of 0 $\text{GPa}\cdot\text{m}^{0.5}/\text{s}$, the weakening influence of pre-shear force on static fracture toughness is exhibited obviously in the Eq. (5).

Based on Eq. (5), an empirical model amongst normalised total fracture toughness K_{IIC}^{tot} and pre-shear as well as the loading rate \dot{K}_{II} can be further acquired.

$$\frac{K_{IIC}^{tot}}{K_{IIC}^s} = f_{tot} \left(\frac{K_{II}^s}{K_{IIC}^s}, \frac{\dot{K}_{II}}{\dot{K}_{II}^s} \right) = \frac{K_{II}^s + K_{IIC}^d}{K_{IIC}^s} = 1 + \alpha \left(\frac{\dot{K}_{II}}{\dot{K}_{II}^s} \right)^\beta \quad (6)$$

To determine the parameters α and β , the data showed in the Fig. 10b are employed to fit the Eq. (6). The fitting result is given by

$$K_{IIc}^{tot} / K_{IIc}^s = 1 + 0.0019 \cdot (\dot{K}_{II} / \dot{K}_{II}^s)^{0.636} (R^2 = 0.9804) \quad (7)$$

It can be found in Fig. 9b that the empirical relation proposed in this study has a good match with K_{IIc}^{tot} under varying APFR and the loading rate. Then the fitting parameters α and β are substituted into Eq. (6) and loading rate $\dot{K}_{II} - K_{IIc}^d$ curves for four APFRs are displayed in the Fig. 10a. The calculation results using the Eq. (6) offer a very satisfactory estimation outcomes compared to the experimental data. Therefore, the empirical model based on the dynamic SCC method has the great potential of estimating dynamic and total mode II fracture toughness for rock subjected to coupled static–dynamic loads.

3.5 Dynamic Fracture Behaviour

3.5.1 Dynamic Damage and Fracture Processes

The 3D DIC technique is an effective approach for monitoring the deformation field on the specimen surface. By means of this method, the surface deformation field during coupled dynamic and static loading on the SCC specimens was obtained from the DIC data. Meanwhile, damage characteristics of the SCC specimen also are analysed according to the apparent principal strain field.

The damage factor, namely standard deviation of principal strain e_1 within ROI, was defined by Song et al. (2013) and Zhu et al. (2021) to describe the damage behaviour during rock dynamic fracture process, which can be calculated by:

$$\bar{e}_1 = \left(\sum_{i=1}^m e_1^i \right) / m \quad (8)$$

$$S(e_1) = \sqrt{\frac{1}{m-1} \sum_{i=1}^m (e_1^i - \bar{e}_1)^2} \quad (9)$$

$$\tilde{S} = S(e_1) / S_{max} \quad (10)$$

where e_1^i represents the maximum principal strain at any point i , m is the total count of data points within the ROI, \bar{e}_1 denotes the average value of e_1^i , S_{max} is the maximum of $S(e_1)$ obtained from the first photograph at the completion of the shear fracture.

The evolution of total SIF and damage factor with time for SCC specimen with a loading rate of $74.14 \text{ GPa}\cdot\text{m}^{0.5}/\text{s}$ at 25% APFR is plotted in Fig. 11. Figure 12 displays the principal strain contours at various total SIF levels, corresponding to points I–VI respectively in Fig. 11.

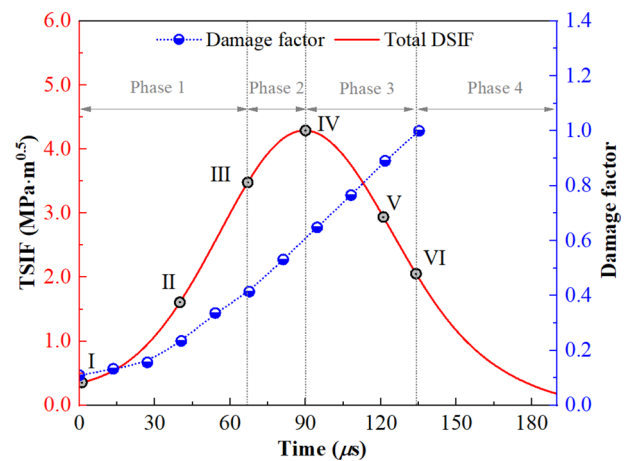
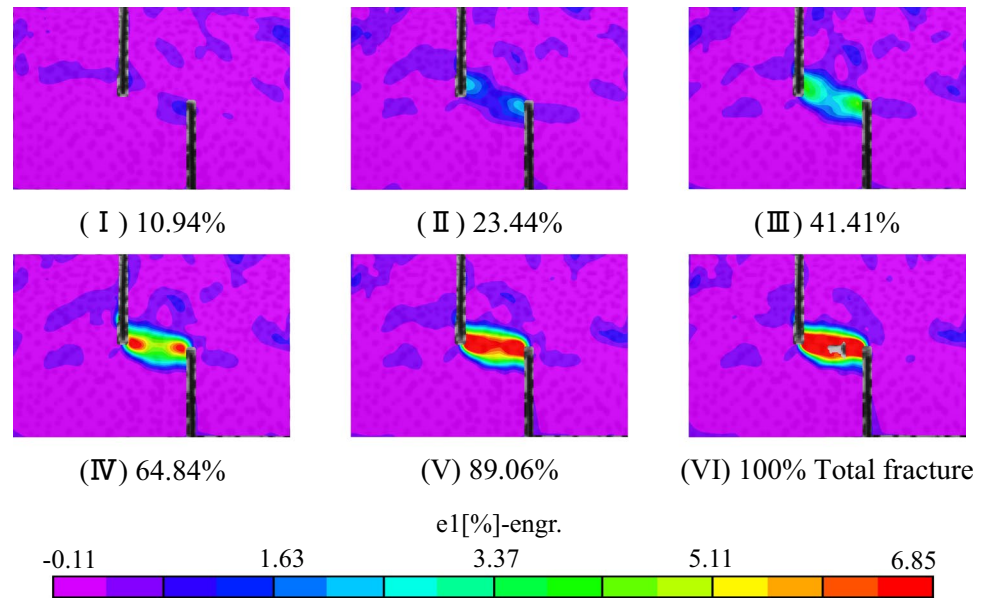


Fig. 11 The variation in TSIF and damage factor with time at 25% APFR

Due to the presence of static pre-force, the SCC specimen is damaged initially up to the 10.94% of damage factor at point I before impact load is applied. It can be noticed in Fig. 12 (I) that a principal strain concentration zone has been first formed at tips of the two notches, although the maximum of principal strain e_{1max} , nearly 0.6%, is relatively small. The TSIF (total stress intensity factor) before point II increased approximately nonlinearly with time after the impact pulse is applied. The damage to the SCC specimen was twice as much as that at point I and reached a damage factor of 23.44%. As shown in Fig. 12 (II), the maximum of principal strain e_{1max} near tips increases to 1.92%. Then the slope of TSIF–time curve is almost constant after point II, which means that the dynamic response of SCC specimen is yet elastic up to point III. Since point III, the TSIF–time curve becomes deviant from a straight line and the damage factor–time curve rises significantly to 41.41%, meaning the initiation and expansion of micro-cracks inside the ESFB cause surface plastic deformation. At point IV, as shown in Fig. 12 (IV), two high strain concentration zones with a maximum strain of 5.05% appear in the two tips as dynamic force raises, accompanied with a damage factor of 64.84%. This can be ascribed to the rapid penetration of micro-cracks and formation of macroscopic cracks, namely the fracture onset, whereafter two high strain concentration zones located in the two tips tend to be linked with each other, implying rapid propagation of macroscopic cracks in a very short period and generation of a shear fracture band. Finally, the SCC specimen is fractured totally into two halves. Based on the above discussion, the dynamic fracture process of the SCC specimen can be separated into four stages, i.e. the

Fig. 12 The major principal strain contours of SCC specimen with the 25% APFR



elastic phase, plastic deformation phase, the unstable crack extension phase and post-fracture phase.

3.5.2 The Effect of Axial Pre-force

Figure 13 shows the evolution of principal strain contours at 0% and 75% APFR. It can be demonstrated that axial pre-force exerts an imperative effect on the effective loading time (ELT), namely the consumed time from the arrival of the stress wave at the specimen end to the complete shear fracture, and the initial damage before impacting. For example, it took 126.33 μs of ELT to undergo shear fracture for the specimen with a about 70 $\text{GPa}\cdot\text{m}^{0.5}/\text{s}$ of loading rate at 0% and 25% APFR. However, only 94.64 μs ELT is required for the specimens with 75 APFR at similar loading rates. Obviously, the ELT lowers with increasing APFR. Moreover, as shown in Fig. 12 (I), Fig. 13a and d, the SCC specimen subjected to sole impact holds a static damage factor of 6.67% before applying the impact load, whilst specimens with APFRs of 25% and 75% have a static damage factor up to 10.94% and 24.15%. This means static damage of SCC specimens increases significantly with the growth in the APFR, and static axial pre-force evidently deteriorates the resistance of the rock to crack initiation and extension. It is noteworthy that the same ELT was spent for specimens under single impact or with 25% APFR, and the specimen acted upon by only single impact load also exhibits some initial damage. It can be attributed to the fact that the relatively large frame rate of HS cameras were used in the study and the small pre-force applied for sandwiching specimens between two bars under sole impact.

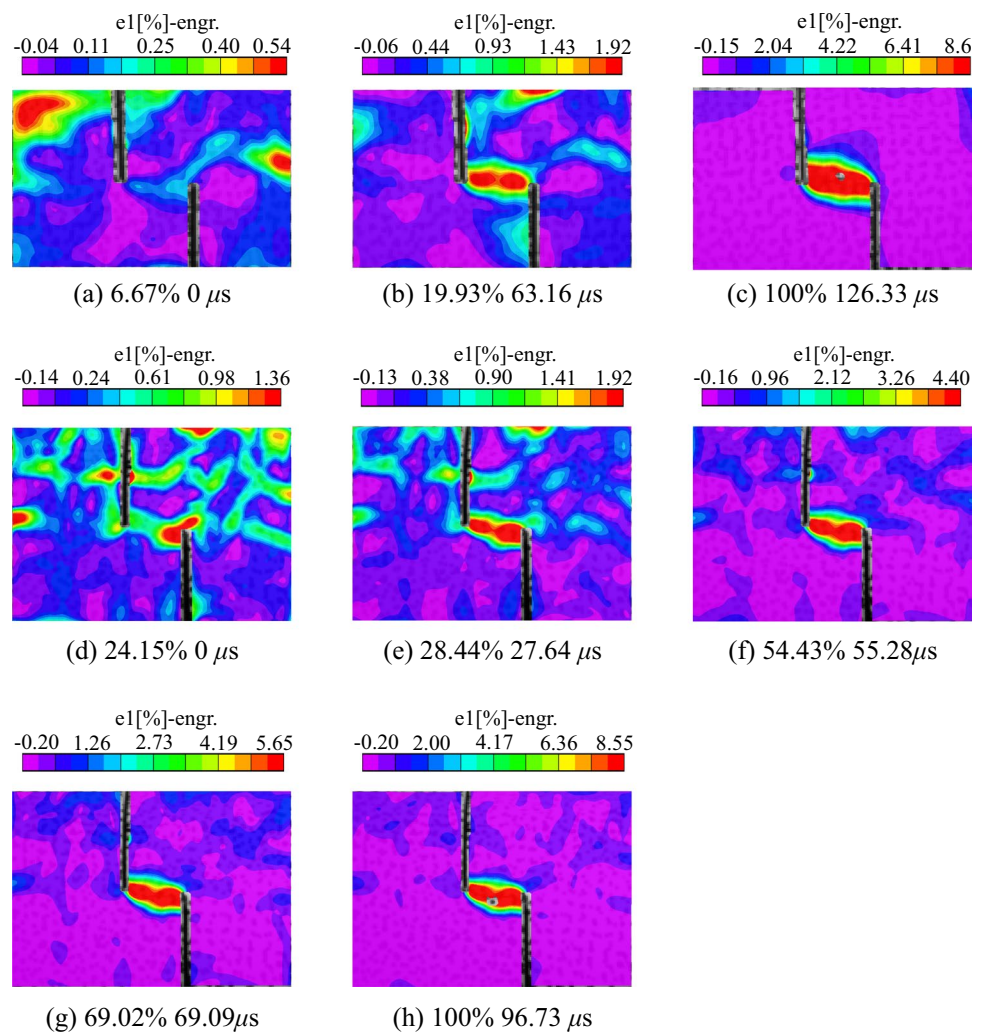
3.5.3 The Effect of Loading Rate

In this part, special attention was paid to the effect of loading rate on the dynamic shear fracture process and failure pattern under same APFR. To avoid repetitive analysis, three typical specimens with different loading rates, namely 58.15, 84.13 and 108.87 $\text{GPa}\cdot\text{m}^{0.5}/\text{s}$ at 50% APFR were selected, which correspond to three representative failure patterns. Their fracture process and the recovered specimens are displayed in the Figs. 14 and 15.

The first obvious phenomenon is that at the given APFR, the increase in loading rate speeds up the ELT of the SCC specimen. For example, overall shear fracture of the specimen with 58.15 $\text{GPa}\cdot\text{m}^{0.5}/\text{s}$ occurred at 151.59 μs , which was accelerated to the time of 101.06 μs and 88.43 μs by specimens with 84.13 and 108.87 $\text{GPa}\cdot\text{m}^{0.5}/\text{s}$.

Besides, the final failure pattern shifts with the loading rate. Figure 14a demonstrates fracture process of the class I failure in SPHB-SCC tests. Obviously, a principal strain first appeared at the tip of right notch at 50.53 μs , indicating rock at this location will be the first to crack, then propagated straight towards the direction normal to the prefabricated notches, forming a near-horizontal shear fracture band. At 151.59 μs , the specimens were entirely broken into two roughly same halves along the ESPB (expected shear fracture band). In the light of the analysis for the entire failure process and the recovered specimens, the class I pattern was the predominant failure pattern in SHPB-SCC tests under low loading rate, namely the loading rate below 70 $\text{GPa}\cdot\text{m}^{0.5}/\text{s}$.

Fig. 13 The principal strain contours of SCC specimens with the 0% (a–c) and 75% (d–h) of axial pre-force ratio



The final failure pattern changes once the loading rate exceed 80 $\text{GPa}\cdot\text{m}^{0.5}/\text{s}$. Figure 14b shows the class II failure process. The preceding part before 106.06 μ s was similar to that for class I failure until 1099.03 μ s, at which a distinct crack away from the tip of right notch was spotted. Then, the secondary fractures further propagated and coalesced, generating three main fragments, as shown in Fig. 14b.

Figure 14c displays the class III failure process for the SCC specimen. The front part before 88.427 μ s was similar to that for class I failure until 972.71 μ s, at which two noticeable cracks initiated from the tips of both notches, were observed in two halves of specimen. Then, the two secondary fractures further propagated towards two ends of the specimen along loading direction, forming several rock fragments. This is very similar to the phenomenon of axial splitting that often occurred at dynamic uniaxial compressive tests (Li et al. 2021a, b; Zhou et al. 2020). It can be ascribed to the fact that for the SCC specimen damaged by axial pre-force, the incident energy from the impact is so large that there is still an amount of remaining energy after

the shear fracture of the specimen is completed. Due to the restricted effect of static pre-force, two fractured rock blocks are squeezed together and two surfaces of each notch are in close contact, forming an approximate cylindrical specimen with some damage. This specimen is acted upon by the remaining energy to induce the axial splitting. Similarly, the secondary fracture in class III failure, occurred on the end, can be explained in the same way. It is noted that class III failure was discovered as the loading rate surpasses 90 $\text{GPa}\cdot\text{m}^{0.5}/\text{s}$.

In general, other pre-force cases also conform to the above pattern, although there are some differences in the loading rate thresholds at which the failure pattern shifts and in the number of rock fragments at ultimate failure.

The principal strain contours in Fig. 14 show the mode II fracture path in SCC specimens appears to be insensitive to the loading rate. The fracture initiated from the crack tips and expanded towards the middle part of the ESFB along a straight line until the occurrence of a shear fracture band. According to the above analysis, three failure patterns were

Fig. 14 Fracture processes with a pre-force ratio of 0.5 at various loading rates: **a** 58.15 GPa·m^{0.5}/s, **b** 84.13 GPa·m^{0.5}/s and **c** 108.87 GPa·m^{0.5}/s

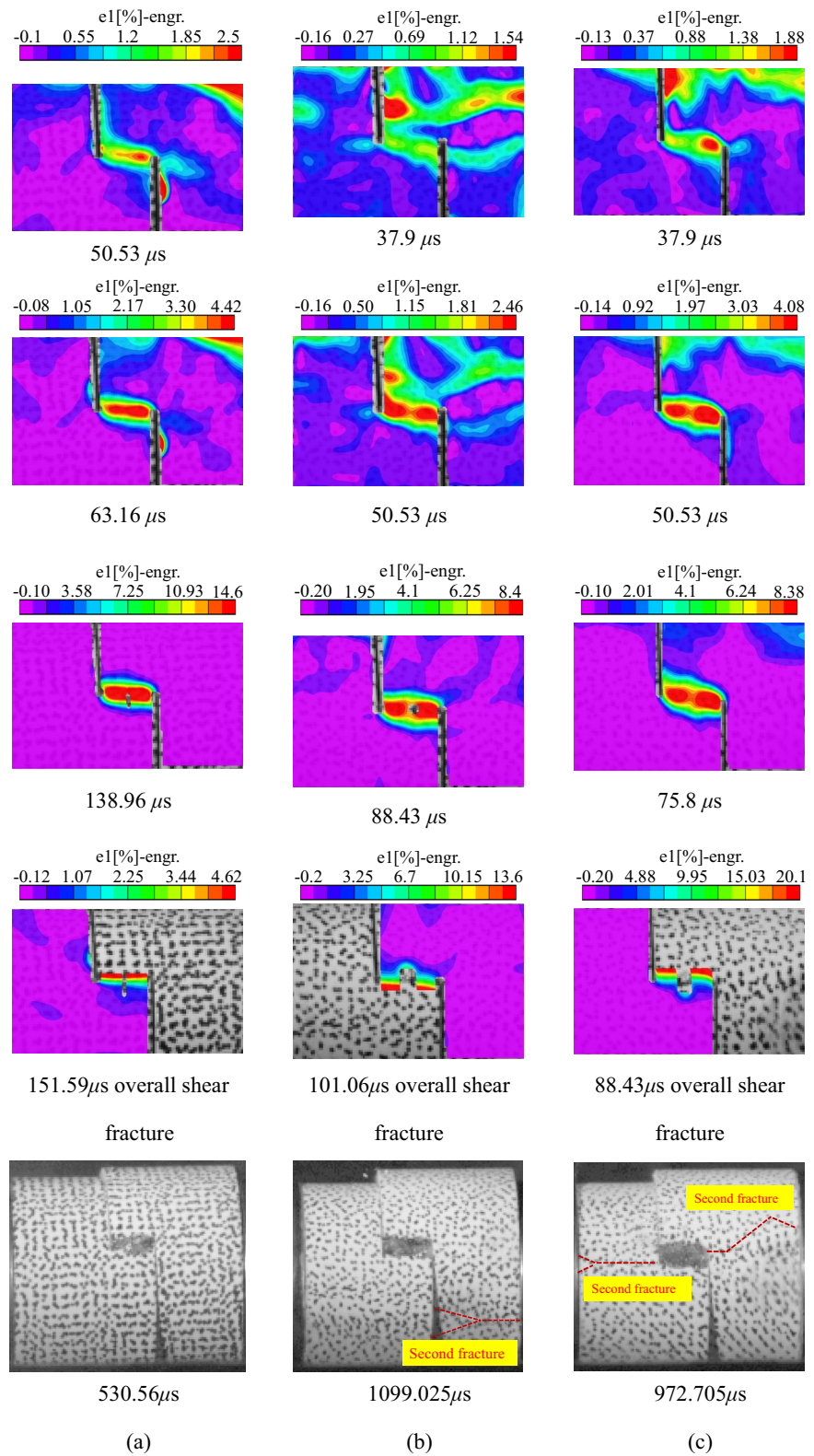
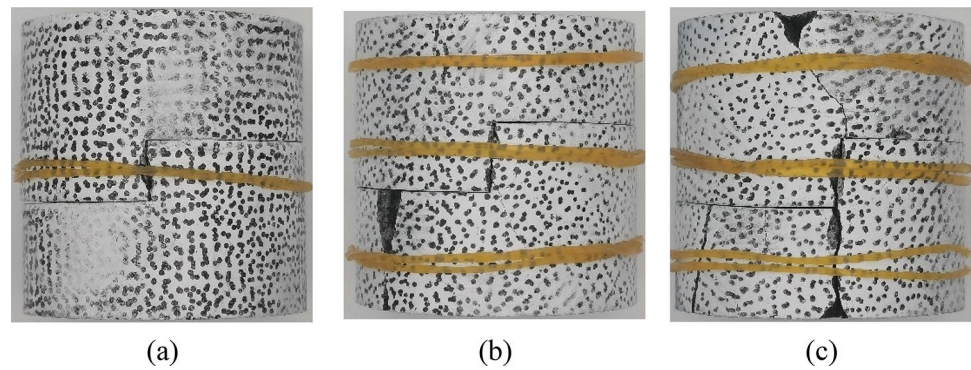


Fig. 15 The recovered samples with a pre-force ratio of 0.5 at various loading rates: **a** 58.15 GPa·m^{0.5}/s, **b** 84.13 GPa·m^{0.5}/s and **c** 108.87 GPa·m^{0.5}/s



essentially compliant to the shear fracture despite some irregular cracks in the specimens following the mode II fracture. This indicates the tests were valid and Eq. (2) could be used in the study.

3.6 Dynamic Deformation Behaviour and Relative Shear Velocity

To further understand dynamic deformation behaviour of SCC specimens under coupled dynamic-static loading, a displacement measuring line (DML, $X=0.66$ mm, $Y=-13.00\sim+13.00$ mm) is laid out along the vertical bisector of the ESFB to record horizontal displacements at different loading moment by 3D-DIC, as shown in Fig. 5. Figure 16 shows variation of horizontal displacement along the DML for the specimen with 75% APFR at a 70 GPa·m^{0.5} of loading rate, corresponding to the principal strain contours shown in Fig. 13d–h respectively. Figure 16 depicts the evolution of horizontal displacement at five loading moments in Fig. 13d–h. In addition, relative shear displacement means the difference in horizontal displacements of both sides of the ESPB.

As illustrated in Fig. 16, the horizontal displacement at 0 μ s is distributed relatively uniformly with Y-coordinates and the discontinuous part is not noticed. The isolines in displacement contour are relatively twisted (Fig. 17a) and no merged point or band emerges at the ESFB, showing that the SCC specimen still behaves as an elastic deformation (Miao et al. 2020; Zhang et al. 2015). At 27.04 μ s, a marked saltation segment in terms of slope in the U–Y curve appears (Fig. 17b), showing that the rock in ESFB begins to experience plastic deformation. The important feature in horizontal displacement was used by many scholars (Lin and Labuz 2013; Ma et al. 2022; Miao et al. 2020; Moazami et al. 2020) to determine the crack initiation and geometrical parameters of the fracture process zone (PFZ) for opening fracture. In this study, the width of shear fracture process zone (SPFZ) for SCC specimen is determined as 5.82 mm, which are verified further by subsequent U–Y curves. Then, with increase in dynamic load, the isolines in

displacement contour concentrate towards the ESFB and the slope of horizontal displacement curve in the region crossing the ESPB obviously increases. A merged band at the ESFB, generated by dense displacement isolines, is detected from Fig. 17c, d and e, manifesting that microcracks inside the ESFB propagate and coalesce fast and a macroscopic shear fracture band forms.

In the methods to determine mode I fracture toughness, the used specimens often have only single notch being pre-fabricated and thus the crack propagation process could be visually observed by ascertaining the location of the crack tip based on apparent displacement field from DIC data. Hence, the crack propagation velocity can be easily measured in dynamic fracture tests according to the distance and time taken for the crack tip to move (Zhou et al. 2019b). However, specimen configurations with double notches, e.g. SCC method (Yao et al. 2020), PTS method (Backers et al. 2002), shear-box method (Rao et al. 2003) and DNBD method (Bahrami et al. 2020), are dominant in the methods for assessing shear fracture toughness. In our previous study,

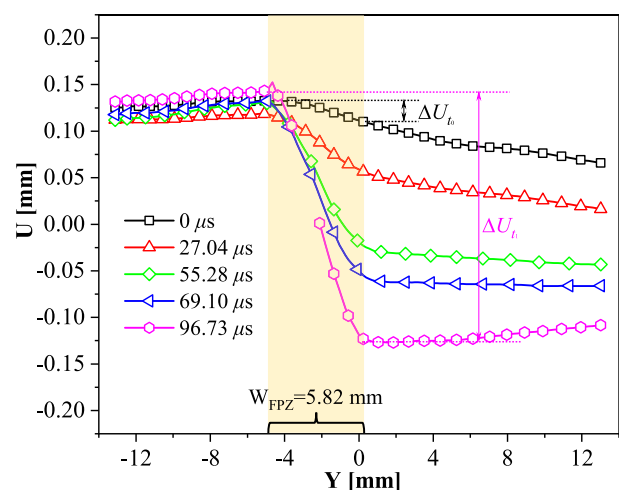
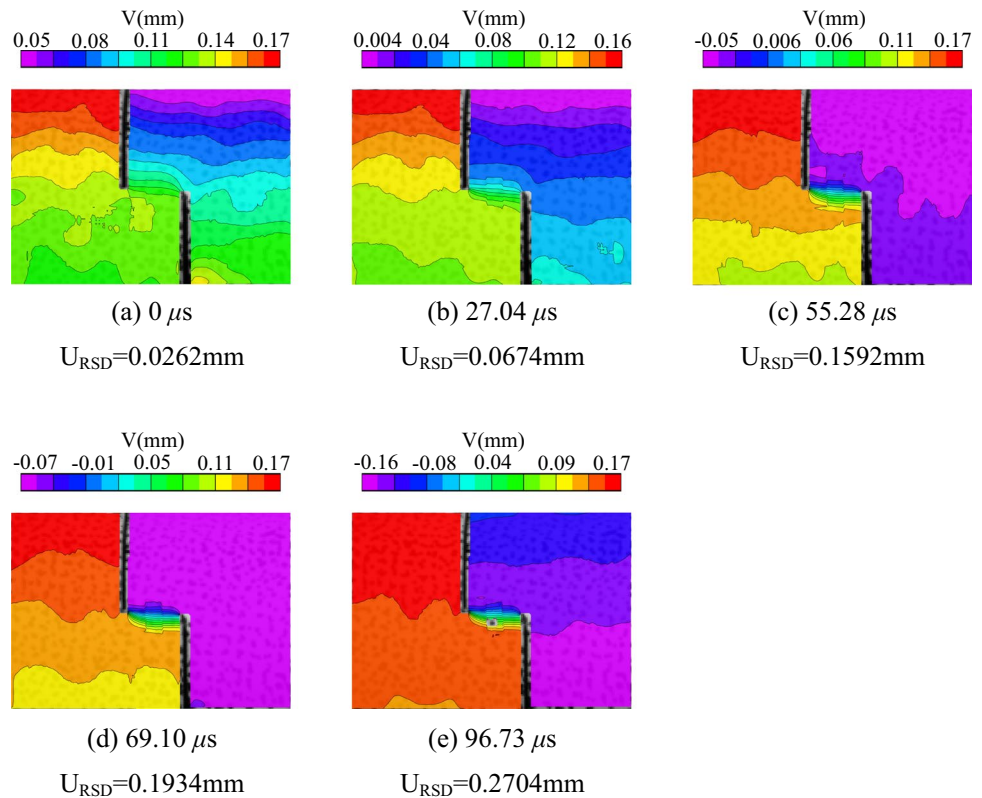


Fig. 16 Horizontal displacement curves at five loading moments, corresponding to the principal strain contours shown in Fig. 12d–h respectively

Fig. 17 The horizontal displacement contours at different moments: **a** 0 μs , **b** 27.04 μs , **c** 55.28 μs , **d** 69.10 μs and **e** 96.73 μs



dynamic deformation and fracture behaviour of granite by the SCC method with 3D DIC were investigated in detail under static loads, in which the consistency and the simultaneity of displacement evolution along ESFB during loading were found. As shown in Fig. 17, this conclusion can be further extended to the conditions of coupled dynamic-static loading. This brings about some difficulties in determining the shear crack propagation velocity since the tip location for the expanding shear crack cannot be accurately determined. To investigate the effect of both pre-force and loading rate on the shear crack propagation, a new index, namely the relative shear velocity (RSV), is proposed, which describes the average relative horizontal velocity of the specimen during the time interval between the deformation onset and complete shear fracture.

As shown in Fig. 16, there is a large horizontal displacement change in the region through the ESPB, so the distance to the acclinic bisector of the ESPB along the direction of applied load is a key factor to influence accuracy of relative shear displacement. The fluctuation of relative shear displacement at right and left boundaries between the FPZ and the elastic zone is relatively small. In addition, considering that the shear fracture band for SCC specimen is approximately horizontal, the variation in FPZ width during loading can be neglected. The relative shear velocity (RSV) can be computed by:

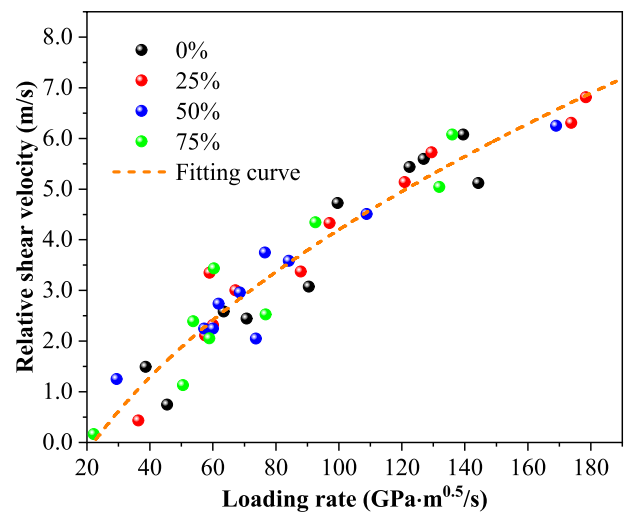


Fig. 18 The relation between the relative shear velocity and loading rate

$$v_{RSV} = (\Delta U_{t_i} - \Delta U_{t_0}) / \Delta t = (|U_{t_i}^1 - U_{t_i}^2| - |U_{t_0}^1 - U_{t_0}^2|) / (t_i - t_0) \tag{11}$$

where $U_{t_i}^1$ and $U_{t_0}^1$ are horizontal displacements of the upper and right part of the ESPB (shown in Fig. 5) within the ROI at time t_i and t_0 , $U_{t_i}^2$ and $U_{t_0}^2$ are horizontal displacements of the lower and left part of the ESPB within the ROI (shown

in Fig. 5) at time t_i and t_0 . $|U_{t_i}^1 - U_{t_i}^2|$ represents the relative shear displacement at time t_i .

Take a specimen with a pre-force ratio of 75% AFSR and a loading rate of $70 \text{ GPa}\cdot\text{m}^{0.5}/\text{s}$ as an example, t_0 is $0 \mu\text{s}$ and t_i is $96.73 \mu\text{s}$. Hence, $U_{t_0}^1 = 0.1328 \text{ mm}$, $U_{t_0}^2 = 0.1066 \text{ mm}$, $U_{t_i}^1 = 0.1436 \text{ mm}$ and $U_{t_i}^2 = -0.1269 \text{ mm}$, relative shear displacements at t_0 and t_i can be calculated as 0.0262 mm and 0.2704 mm . According to the Eq. (11), v_{RSV} can be determined as 2524.63 mm/s . Then, as depicted in Fig. 18, based on the above method, we obtained the v_{RSV} of other specimens with different pre-shear ratio and loading ratio. Evidently, v_{RSV} increases with growth in loading rate, with the relation to be the power function. The fitting result is given by:

$$v_{RSV} = 0.8174 \dot{K}_{II}^{0.4948} - 3.781 \quad (R^2 = 0.9203) \quad (12)$$

In addition, the effect of the axial pre-force ratio (ASPR) on v_{RSV} appears to be ambiguous.

4 Discussion

In Sect. 3.2, a rate-dependence of mode II fracture toughness was obtained. It can be explained by the micro-morphological features of shear fracture surfaces. In our recent study, it was found that trans-granular fracture (TG) was more common at high loading rates by the scanning electron microscope (SEM) observation, compared to intergranular fracture (IG) fracture, which often occurs under static loading. It should be noted that TG fracture of crystalline rocks consumes more energy than IG fracture (Abdollahi and Arias 2012; Lim et al. 2012). Moreover, the rate-dependence is related to the final failure pattern of SCC specimens. Impact load with higher loading rates favours the formation of splitting cracks and secondary cracks, causing an increase in energy consumption.

In Sect. 3.2, the present results indicate that at similar loading rates, the magnitude of pre-force has almost no effect on total mode II fracture toughness, which are consistent with the results of other references (Wu et al. 2015; Yao et al. 2019, 2022; Li et al. 2023). However, some investigators (Chen et al. 2016; Han et al. 2022a, b, c; Pei et al. 2020) found that total fracture toughness and tensile strength increase with increment of pre-force. This may be related to the sensitivity of the pre-forced rock materials to the loading rate. The applied axial pre-force induces some microcracks within the rock, leading it a more viscous material and more sensitive to the loading rate. The total fracture toughness is shown to be independent of axial pre-force because the increasing effect of the loading rate

on the fracture toughness compensates for the weakening effect of the pre-force. The increasing total fracture toughness with the growth in pre-force can be ascribed to the fact that the enhancing effect of fracture toughness induced by high sensitivity to loading rate exceeds the deteriorating effect of pre-force and thus total fracture toughness shows an increasing trend.

It can be observed in Fig. 18, the index RSV exhibits a clear rate-dependency, which are similar with the rate effect of crack propagation velocity (CPV) in dynamic mode I fracture. It can be inferred that although the RSV is not a direct measure of shear crack propagation velocity (SCPV), it has the potential to qualitatively reflect rate effect of the SCPV. Fault slip rate in the field of geophysics, at which fracture propagates over the fault, is a concept similar to relative shear velocity and is of enormous significance for the reason that this parameter is closely related to the formation of seismic waves (Sainoki and Mitri 2014). The seismic waves originating from fault slip sometimes lead to the significant damage to mining openings (Sainoki and Mitri 2015a). The slip rate of fault affected by plate movement is generally mm/year (d'Alessio et al. 2005; Savage et al. 1999), whereas the maximum slip rate of fault triggered by sudden earthquake (Bizzarri 2012; Yomogida and Nakata 1994) or underground mining activities (Sainoki and Mitri 2014, 2015a), e.g. blasting, can increase to the m/s. Sainoki and Mitri (2014) examined several factors, e.g. the friction angle and the position of the fault as well as mining depth, which could have an impact on the slip rate of the fault slip using 3D dynamic numerical modelling. Their results suggested that the maximum slip rate on the fault concentrates in the range of $1 \sim 6 \text{ m/s}$ under dynamic load (Sainoki and Mitri 2015b; Sainoki et al. 2017). Recently, Yao et al. (2021a) conducted a series of impact shear tests on the rectangular thin plate specimens with a smooth discontinuity and found peak slip velocity during dynamic loading was on the order of m/s under the normal stress of $0\text{--}20 \text{ MPa}$ and various loading rate. Subsequently, Wang et al. (2022) and Wang et al. (2021) further considered the variation in discontinuity roughness, and found peak slip velocity was in the range from 0.5 to 12 m/s . From the above discussion, it can be seen that the fault slip rate obtained from the numerical simulations regarding mining-induced fault slip and slip velocity from dynamic shear tests for rock discontinuity is consistent with the results in terms of the RSV in this study.

5 Implications

The present experimental indicates that pre-force has a significant weakening effect on dynamic mode II fracture toughness. This enlightens us that in mining engineering, the design of blasting schemes should consider the effect of geostress. On the one hand, the impact load generated by less explosives can also cause crack propagation and achieve the purpose of fragmentation of rock or ore drawing at higher geostress than at lower geostress. On the other hand, the dynamic load by blasting is transferred to the peripheral rock to promote the propagation of cracks, increasing the risk of instability of surrounding rock at mining roadways. Moreover, the dynamic loads also have a large impact on the stability of pre-stressed support structures in deep mining engineering, such as ore pillars. This is because the capacity of the support structure to resist crack propagation under dynamic load has been significantly weakened by the geostress in the vertical direction and cracks in support structures can easily propagate under the disturbance of dynamic load.

6 Conclusions

In this work, a coupled static–dynamic loading system with a SCC specimen was employed to evaluate the dynamic mode II fracture toughness of rocks subjected to different pre-forces. Four groups of specimens are measured under a pre-force of 0, 0.25, 0.5, and 0.75 static peak loads with extensive dynamic loading rates. The surface strain field and the displacement field on the specimens were investigated during fracture processes by virtue of the dynamic 3D-DIC technique. The main conclusions are listed below:

- (1) At the same pre-force ratio, there is a clear trend of increasing dynamic mode II fracture toughness of rock as the loading rate raises. The dynamic mode II fracture toughness declines with the increase of the pre-force ratio at a given loading rate because of original damage induced by the pre-force before impact. In addition, total mode II fracture toughness is approximately insensitive to the pre-force ratio.
- (2) An empirical model is introduced to demonstrate the impact of the pre-force ratio and loading rate. The result shows that the empirical formula can well characterise the relationship amongst dynamic mode II fracture toughness, total mode II fracture toughness with respect to pre-force ratio and loading rate.
- (3) The original damage caused by static pre-force before impact augments with the pre-force ratio. The dynamic fracture path seems to be independent of pre-force and loading rate in the studied range. At higher pre-force

and loading rate, the time to achieve overall shear fracture is reduced. At a given pre-force ratio, the final failure pattern of the SCC specimen is significantly influenced by the loading rate.

- (4) Based on displacement field, a new index, namely the relative shear velocity (RSV), defined as the ratio of relative shear displacement and time taken from deformation onset to complete fracture, is proposed to depict the influence of both pre-force ratio and loading rate on shear fracture propagation. The results imply that the RSV increases with loading rate regardless of the pre-force ratio, with the relation of power function, whereas this index seems to be also independent of pre-force ratio.

Acknowledgements The present research was financially supported by the National Natural Science Foundation of China (52074349) and the Fundamental Research Funds for Central Universities of the Central South University (No.2022ZZTS0309).

Data availability statement The data that support the findings of this study are available from the corresponding author upon reasonable request.

Declarations

Conflict of Interest The authors declare that they have no conflict of interests.

References

- Abdollahi A, Arias I (2012) Numerical simulation of intergranular and transgranular crack propagation in ferroelectric polycrystals. *Int J Fract* 174:3–15
- Aliabadian Z, Zhao GF, Russell AR (2019) Crack development in transversely isotropic sandstone discs subjected to Brazilian tests observed using digital image correlation. *Int J Rock Mech Min Sci* 119:211–221
- Awaji H, Sato S (1978) Combined mode fracture toughness measurement by the disk test. *J Eng Mater Technol* 100:175–182
- Ayatollahi M, Aliha M (2011) On the use of an anti-symmetric four-point bend specimen for mode II fracture experiments. *Fatigue Fract Eng Mater Struct* 34:898–907
- Backers T, Stephansson O (2012) ISRM suggested method for the determination of mode II fracture toughness. *Rock Mech Rock Eng* 45:1011–1022
- Backers T, Stephansson O, Rybacki E (2002) Rock fracture toughness testing in Mode II—punch-through shear test. *Int J Rock Mech Min Sci* 39:755–769
- Bahrami B, Nejati M, Ayatollahi MR, Driesner T (2020) Theory and experiment on true mode II fracturing of rocks. *Eng Fract Mech* 240:107314
- Bahrami B, Ghoulis S, Nejati M, Ayatollahi MR, Driesner T (2022) Size effect in true mode II fracturing of rocks: theory and experiment. *Eur J Mech A* 94:104593

- Bizzarri A (2012) Rupture speed and slip velocity: what can we learn from simulated earthquakes? *Earth Planet Sci Lett* 317:196–203
- Cai X, Zhou Z, Tan L, Zang H, Song Z (2020) Fracture behavior and damage mechanisms of sandstone subjected to wetting-drying cycles. *Eng Fract Mech* 234:107109
- Chen R, Li K, Xia K, Lin Y, Yao W, Lu F (2016) Dynamic fracture properties of rocks subjected to static pre-load using notched semi-circular bend method. *Rock Mech Rock Eng* 49:3865–3872
- Cho SH, Ogata Y, Kaneko K (2003) Strain-rate dependency of the dynamic tensile strength of rock. *Int J Rock Mech Min Sci* 40:763–777
- Dai F, Chen R, Xia K (2010) A semi-circular bend technique for determining dynamic fracture toughness. *Exp Mech* 50:783–791
- d'Alessio M, Johanson I, Bürgmann R, Schmidt D, Murray M (2005) Slicing up the San Francisco Bay area: block kinematics and fault slip rates from GPS-derived surface velocities. *J Geophys Res* 110:B6
- Du S, Li D, Ruan B, Wu G, Pan B, Ma J (2020) Deformation and fracture of circular tunnels under non-tectonic stresses and its support control. *Eur J Environ Civ En* 26:1654–1677
- Du S, Li D, Zhang C, Mao D, Ruan B (2021) Deformation and strength properties of completely decomposed granite in a fault zone. *Geomech Geophys Geo* 7:1–21
- Erdogan F, Sih GC (1963) On the crack extension in plates under plane loading and transverse shear. *J Basic Eng* 85:519–525
- Esterhuizen G, Dolinar D, Ellenberger J (2011) Pillar strength in underground stone mines in the United States. *Int J Rock Mech Min Sci* 48:42–50
- Han Z, Li D, Li X (2022a) Dynamic mechanical properties and wave propagation of composite rock-mortar specimens based on SHPB tests. *Int J Min Sci Technol*. <https://doi.org/10.1016/j.ijmst.2022.05.008>
- Han Z, Li D, Li X (2022b) Effects of axial pre-force and loading rate on Mode I fracture behavior of granite. *Int J Rock Mech Min Sci* 157:105172
- Han Z, Li D, Li X (2022c) Experimental study on the dynamic behavior of sandstone with coplanar elliptical flaws from macro, meso, and micro viewpoints. *Theor Appl Fract Mech* 120:103400
- Li X, Zhou Z, Lok T-S, Hong L, Yin T (2008) Innovative testing technique of rock subjected to coupled static and dynamic loads. *Int J Rock Mech Min Sci* 45:739–748
- Li D, Li B, Han Z, Zhu Q, Liu M (2021a) Evaluation of Bi-modular behavior of rocks subjected to uniaxial compression and Brazilian tensile testing. *Rock Mech Rock Eng* 54:3961–3975
- Li X, Gu H, Tao M, Peng K, Cao W, Li Q (2021b) Failure characteristics and meso-deterioration mechanism of pre-stressed coal subjected to different dynamic loads. *Theor Appl Fract Mec* 115:103061
- Li D, Zhang C, Zhu Q, Ma J, Gao F (2022) Deformation and fracture behavior of granite by the short core in compression method with 3D digital image correlation. *Fatigue Fract Eng Mater Struct* 45:425–440
- Li Y, Dai F, Liu Y, Wei M (2023) Effects of pre-static loads on the dynamic pure mode I and mixed mode I-II fracture characteristics of rocks. *Eng Fract Mech* 279:109047
- Lim SS, Martin CD, Åkesson U (2012) In-situ stress and microcracking in granite cores with depth. *Eng Geol* 147:1–13
- Lin Q, Labuz JF (2013) Fracture of sandstone characterized by digital image correlation. *Int J Rock Mech Min Sci* 60:235–245
- Ma J, Li D, Zhu Q, Liu M, Wan Q (2022) The mode I fatigue fracture of fine-grained quartz-diorite under coupled static loading and dynamic disturbance. *Theor Appl Fract Mec* 117:103140
- Miao S, Pan P, Yu P, Zhao S, Shao C (2020) Fracture analysis of Beishan granite after high-temperature treatment using digital image correlation. *Eng Fract Mech* 225:106847
- Moazzami M, Ayatollahi M, Akhavan-Safar A (2020) Assessment of the fracture process zone in rocks using digital image correlation technique: the role of mode-mixity, size, geometry and material. *Int J Damage Mech* 29:646–666
- Munoz H, Taheri A (2017) Specimen aspect ratio and progressive field strain development of sandstone under uniaxial compression by three-dimensional digital image correlation. *J Rock Mech Geotech* 9:599–610
- Munoz H, Taheri A, Chanda E (2016) Pre-peak and post-peak rock strain characteristics during uniaxial compression by 3D digital image correlation. *Rock Mech Rock Eng* 49:2541–2554
- Niu C, Zhu Z, Zhou L, Li X, Ying P, Dong Y, Deng S (2021) Study on the microscopic damage evolution and dynamic fracture properties of sandstone under freeze-thaw cycles. *Cold Reg Sci Technol* 191:103328
- Pei P, Dai F, Liu Y, Wei M (2020) Dynamic tensile behavior of rocks under static pre-tension using the flattened Brazilian disc method. *Int J Rock Mech Min Sci* 126:104208
- Peng K, Lv H, Zou Q, Wen Z, Zhang Y (2020) Evolutionary characteristics of mode-I fracture toughness and fracture energy in granite from different burial depths under high-temperature effect. *Eng Fract Mech* 239:107306
- Pook LP (1971) The effect of crack angle on fracture toughness. *Eng Fract Mech* 3:205–218
- Rao Q, Sun Z, Stephansson O, Li C, Stillborg B (2003) Shear fracture (Mode II) of brittle rock. *Int J Rock Mech Min Sci* 40:355–375
- Sainoki A, Mitri HS (2014) Dynamic behaviour of mining-induced fault slip. *Int J Rock Mech Min Sci* 66:19–29
- Sainoki A, Mitri HS (2015a) Effect of slip-weakening distance on selected seismic source parameters of mining-induced fault-slip. *Int J Rock Mech Min Sci* 73:115–122
- Sainoki A, Mitri HS (2015b) Evaluation of fault-slip potential due to shearing of fault asperities. *Can Geotech J* 52:1417–1425
- Sainoki A, Mitri HS, Chinnasane D (2017) Characterization of aseismic fault-slip in a deep hard rock mine through numerical modeling: case study. *Rock Mech Rock Eng* 50:2709–2729
- Savage J, Svarc J, Prescott W (1999) Geodetic estimates of fault slip rates in the San Francisco Bay area. *J Geophys Res* 104:4995–5002
- Shi D, Chen X (2018) Flexural tensile fracture behavior of pervious concrete under static preloading. *J Mater Civil Eng* 30:06018015
- Song H, Zhang H, Fu D, Kang Y, Huang G, Qu C, Cai Z (2013) Experimental study on damage evolution of rock under uniform and concentrated loading conditions using digital image correlation. *Fatigue Fract Eng Mater Struct* 36:760–768
- Tang Z, Liang J, Xiao Z, Guo C (2012) Large deformation measurement scheme for 3D digital image correlation method. *Opt Laser Eng* 50:122–130
- Wang F, Xia K, Yao W, Wang S, Wang C, Xiu Z (2021) Slip behavior of rough rock discontinuity under high velocity impact: Experiments and models. *Int J Rock Mech Min Sci* 144:104831
- Wang F, Wang S, Yao W, Li X, Meng F, Xia K (2022) Effect of roughness on the shear behavior of rock joints subjected to impact loading. *J Rock Mech Geotech*. <https://doi.org/10.1016/j.jrmge.2022.04.011>
- Wei M, Dai F, Xu N, Zhao T, Xia K (2016) Experimental and numerical study on the fracture process zone and fracture toughness determination for ISRM-suggested semi-circular bend rock specimen. *Eng Fract Mech* 154:43–56
- Wei M, Dai F, Xu N, Zhao T, Liu Y (2017) An experimental and theoretical assessment of semi-circular bend specimens with chevron and straight-through notches for mode I fracture toughness testing of rocks. *Int J Rock Mech Min Sci* 99:28–38
- Wu B, Chen R, Xia K (2015) Dynamic tensile failure of rocks under static pre-tension. *Int J Rock Mech Min Sci* 80:12–18

- Wu Y, Yin T, Tan X, Zhuang D (2021) Determination of the mixed mode I/II fracture characteristics of heat-treated granite specimens based on the extended finite element method. *Eng Fract Mech* 252:107818
- Xing H, Zhang Q, Ruan D, Dehkhoda S, Lu G, Zhao J (2018) Full-field measurement and fracture characterisations of rocks under dynamic loads using high-speed three-dimensional digital image correlation. *Int J Impact Eng* 113:61–72
- Yao W, Xu Y, Yu C, Xia K (2017) A dynamic punch-through shear method for determining dynamic mode II fracture toughness of rocks. *Eng Fract Mech* 176:161–177
- Yao W, Xia K, Jha AK (2019) Experimental study of dynamic bending failure of Laurentian granite: loading rate and pre-load effects. *Can Geotech J* 56:228–235
- Yao W, Xu Y, Xia K, Wang S (2020) Dynamic mode II fracture toughness of rocks subjected to confining pressure. *Rock Mech Rock Eng* 53:569–586
- Yao W, Wang C, Xia K, Zhang X (2021a) An experimental system to evaluate impact shear failure of rock discontinuities. *Rev Sci Instrum* 92:034501
- Yao W, Xu Y, Wang C, Xia K, Hokka M (2021b) Dynamic Mode II fracture behavior of rocks under hydrostatic pressure using the short core in compression (SCC) method. *Int J Min Sci Techno* 31:927–937
- Yao W, Wang J, Wu B, Xu Y, Xia K (2022) Dynamic mode II fracture toughness of rocks subjected to various in situ stress conditions. *Rock Mech Rock Eng* 56(3):2293–2310
- Yin T, Li X, Xia K, Huang S (2012) Effect of thermal treatment on the dynamic fracture toughness of Laurentian granite. *Rock Mech Rock Eng* 45:1087–1094
- Yin T, Tan X, Wu Y, Yang Z, Li M (2021) Temperature dependences and rate effects on Mode II fracture toughness determined by punch-through shear technique for granite. *Theor Appl Fract Mech* 114:103029
- Yin T, Yang Z, Wu Y, Tan X, Li M (2022) Experimental investigation on the effect of open fire on the tensile properties and damage evolution behavior of granite. *Int J Damage Mech*. <https://doi.org/10.1177/10567895221092168>
- Yomogida K, Nakata T (1994) Large slip velocity of the surface rupture associated with the 1990 Luzon earthquake. *Geophys Res Lett* 21:1799–1802
- Zhang J (2019) Two methods for determining dynamic mode-II fracture toughness of rocks. Dissertation, University of Toronto
- Zhang Z, Kou S, Yu J, Yu Y, Jiang L, Lindqvist P (1999) Effects of loading rate on rock fracture. *Int J Rock Mech Min Sci* 36:597–611
- Zhang Z, Kou S, Jiang L, Lindqvist P-A (2000) Effects of loading rate on rock fracture: fracture characteristics and energy partitioning. *Int J Rock Mech Min Sci* 37:745–762
- Zhang H, Fu D, Song H, Kang Y, Huang G, Qi G, Li J (2015) Damage and fracture investigation of three-point bending notched sandstone beams by DIC and AE techniques. *Rock Mech Rock Eng* 48:1297–1303
- Zhang C, Li D, Wang C, Ma J, Zhou A, Xiao P (2022) Effect of confining pressure on shear fracture behavior and surface morphology of granite by the short core in compression test. *Theor Appl Fract Mech*. <https://doi.org/10.1016/j.tafmec.2022.103506>
- Zhang C, Li D, Ma J, Zhu Q, Luo P, Chen Y, Han M (2023) Dynamic shear fracture behavior of rocks: insights from three-dimensional digital image correlation technique. *Eng Fract Mech* 277:109010
- Zhou YX, Xia K, Li X et al (2012) Suggested methods for determining the dynamic strength parameters and mode-I fracture toughness of rock materials. *Int J Rock Mech Min Sci* 49:105–112. <https://doi.org/10.1016/j.ijrmms.2011.10.004>
- Zhou Z, Li X, Zou Y, Jiang Y, Li G (2014) Dynamic Brazilian tests of granite under coupled static and dynamic loads. *Rock Mech Rock Eng* 47:495–505
- Zhou X, Wang Y, Zhang J, Liu F (2019a) Fracturing behavior study of three-flawed specimens by uniaxial compression and 3D digital image correlation: sensitivity to brittleness. *Rock Mech Rock Eng* 52:691–718
- Zhou Z, Cai X, Ma D, Du X, Chen L, Wang H, Zang H (2019b) Water saturation effects on dynamic fracture behavior of sandstone. *Int J Rock Mech Min Sci* 114:46–61
- Zhou Z, Cai X, Li X, Cao W, Du X (2020) Dynamic response and energy evolution of sandstone under coupled static–dynamic compression: insights from experimental study into deep rock engineering applications. *Rock Mech Rock Eng* 53:1305–1331
- Zhu Q, Ma C, Li X, Li D (2021) Effect of filling on failure characteristics of diorite with double rectangular holes under coupled static–dynamic loads. *Rock Mech Rock Eng* 54:2741–2761
- Zhu Q, Li C, Li X, Li D, Wang W, Chen J (2022a) Fracture mechanism and energy evolution of sandstone with a circular inclusion. *Int J Rock Mech Min Sci* 155:105139. <https://doi.org/10.1016/j.ijrmms.2022.105139>
- Zhu Q, Li D, Han Z, Xiao P, Li B (2022b) Failure characteristics of brittle rock containing two rectangular holes under uniaxial compression and coupled static–dynamic loads. *Acta Geotech* 17:131–152
- Zuo J, Huang Y, Liu L (2013) Investigation on meso-fracture mechanism of basalt with offset notch based on in-situ three-point bending tests. *Chin J Rock Mech Eng* 32:740–746

Publisher's Note Springer Nature remains neutral with regard to jurisdictional claims in published maps and institutional affiliations.

Springer Nature or its licensor (e.g. a society or other partner) holds exclusive rights to this article under a publishing agreement with the author(s) or other rightsholder(s); author self-archiving of the accepted manuscript version of this article is solely governed by the terms of such publishing agreement and applicable law.